Liquation Mechanisms in Multicomponent Aluminum Alloys during Welding

Three mechanisms cover most, if not all, wrought aluminum alloys and, for a given alloy and temper, the mechanism can vary from heat to heat

BY C. HUANG AND S. KOU

ABSTRACT. The mechanisms by which liquation is initiated in the partially melted zone of wrought, multicomponent aluminum alloys during welding were studied using three representative liquation-susceptible alloys 2024, 6061 and 7075 as examples. Three different liquation mechanisms were identified. In Mechanism I, which is for alloys beyond the solid solubility limit, liquation-inducing particles are always present and liquation can occur at any heating rate. In Mechanism II, for alloys within the limit but with the particles, liquation requires high heating rates. In Mechanism III, for alloys within the limit and without the particles, liquation occurs when the matrix starts to melt. These three mechanisms cover most, if not all, wrought aluminum alloys since an alloy is either beyond or within the limit. Ternary phase diagrams were found a useful approximation for checking if the alloys were within or beyond the limit. Alloy 7075, which contained liquation-inducing $CuMgAl_2$ particles and Cu_2FeAl_7 coatings on Fe-rich particles, was well within the limit and it liquated by Mechanism II. Alloy 6061 was also within the limit, but the mechanism depended on whether the solution heat treatment of the heat was thorough enough to dissolve liquation-inducing Si-rich particles. If so, it liquated by Mechanism III; if not, by Mechanism II. Alloy 2024, which contained liquation-inducing $CuAl_2$ particles, was near the limit and liquated by Mechanism I if the heat was beyond the limit and by Mechanism II if within. The liquation reactions caused by these particles or coatings were identified. Liquation-induced grain boundary segregation was severe, suggesting severe degradation of mechanical properties, as demonstrated in binary alloy 2219.

C. HUANG and S. KOU are respectively, Graduate Student and Professor in the Department of Materials Science and Engineering, University of Wisconsin-Madison, Wis.

Introduction

The partially melted zone (PMZ) is a region immediately outside the weld metal where liquation can occur during welding and lead to hot cracking and degradation of mechanical properties (Ref. 1). Since the 1950s, liquation and liquation-induced hot cracking in aluminum alloys have been studied extensively, and alloys 2024, 6061, and 7075 are among the most frequently investigated materials (Refs. 2–12). Attention appears to have been focused much more on liquation-induced hot cracking than liquation itself. Optical micrographs of the PMZ showed dark-etching grain boundaries (GBs) as evidence of GB liquation, but without further microstructural details. Liquation mechanisms were often not discussed, the solidification of GB liquid was not studied, and the resultant GB segregation was not measured.

Recently, Huang and Kou (Refs. 13–15) studied PMZ liquation in GMA welds of alloy 2219. This was a binary alloy of about Al-6.3 wt-% Cu, with an Al-rich α matrix and θ ($CuAl_2$) particles. Large θ particles were present in the grain interior and sometimes at the GBs, and small θ particles were observed along the GB. To help discussion later in this report, the most significant results are briefly described below.

First, liquation was initiated at the eutectic temperature by the eutectic reaction between the α matrix and the θ particles to form the eutectic liquid. Unlike the constitutional liquation mechanism proposed by Pepe and Savage for maraging steels (Refs. 16, 17), rapid heating is not required for liquation to occur. This is because in alloy 2219, the θ particles are thermodynamically stable all the way to the eutectic temperature. The closer to the fusion boundary, the higher the peak temperature and the more adjacent α matrix dissolved in the eutectic liquid, and it turned it into a hypoeutectic liquid.

Second, GB liquid solidified with a planar mode and with severe solute segregation. Besides a dark-etching eutectic GB, a distinct light-etching α band, in fact, existed along the GB. This microstructure clearly suggests the hypoeutectic GB liquid solidified with a planar solidification front, first as a soft and ductile solute-depleted α band and last as a hard, brittle solute-rich eutectic at the new GB. This was confirmed by both microsegregation measurements and microhardness testing after welding.

Third, solidification of GB liquid was directional — upward and toward the weld because of the high-temperature gradients in the PMZ.

Fourth, while the soft ductile α band yielded under tensile loading, the brittle GB eutectic fractured into pieces, thus explaining the dramatic strength and ductility losses of the PMZ in tensile testing after welding. The liquation of the large θ particles in the grain interior and the subsequent solidification of the liquid resulted in large eutectic particles and an α ring surrounding each particle. While the ductile α rings yielded under tensile loading, the large brittle eutectic particles fractured into pieces just like the GB eutectic.

Work on the binary alloy 2219 has greatly improved fundamental understanding of liquation and solidification in the PMZ of aluminum welds. However, most commercial aluminum alloys are

KEY WORDS

Aluminum Alloys
Grain Boundaries
Hot Cracking
Liquation
Solidification

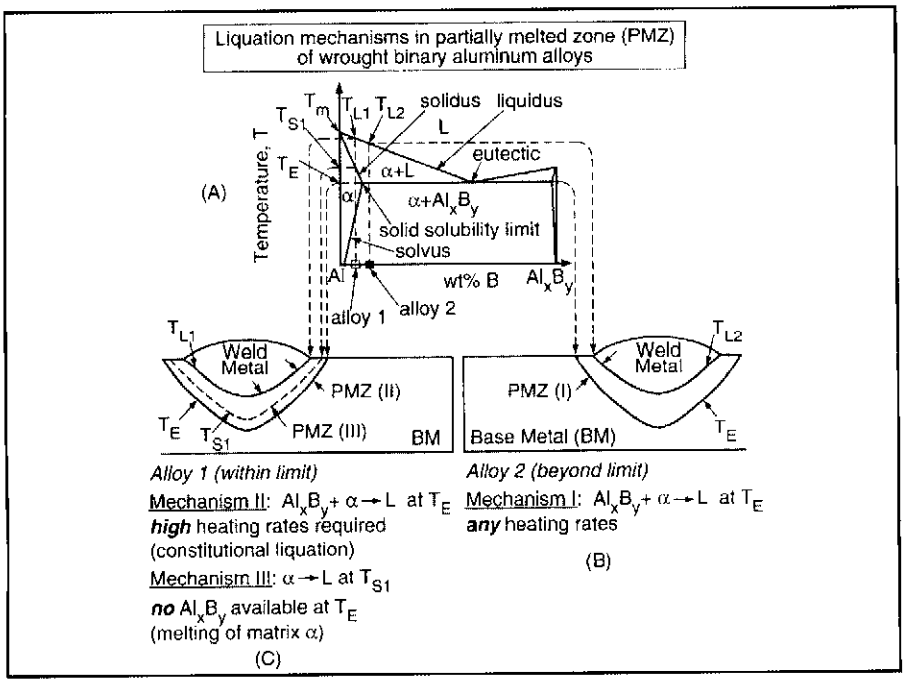

Fig. 1 — Liquation mechanisms in the partially melted zone of wrought binary aluminum alloys. A — Phase diagram; B — Mechanism I; C — Mechanisms II and III.

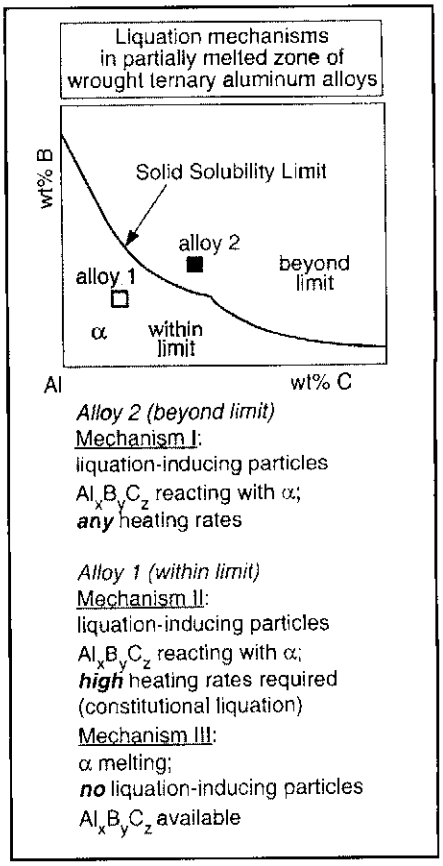

Fig. 2 — Liquation mechanisms in the partially melted zone of wrought ternary aluminum alloys.

multicomponent and it is essential their liquation mechanisms be understood. Unfortunately, this has not been done so far because multicomponent aluminum alloys are much more difficult to understand.

The purpose of the present study is to extend understanding of liquation in alloy 2219 to wrought multicomponent aluminum alloys. The three representative liquation-susceptible alloys, 2024, 6061, and 7075, are selected. To help understand the liquation mechanisms in these alloys, relevant heat treating literature is cited and ternary phase diagrams are used as an approximation. To identify the liquation-inducing particles and the liquation reactions involved, compositions of both particles in the base metal and particles and grain boundaries in the PMZ are determined. Liquation-induced grain boundary segregation is also determined.

Experimental Procedure

The three commercial aluminum alloys studied were alloys 2024-T351, 6061-T651, and 7075-T651. T3 stands for solution heat treating and cold working followed by natural aging. T6 stands for solution heat treating and then artificial aging. T51 stands for stress relieving by stretching (Ref. 18). Actual compositions of the alloys are listed in Table 1 with nominal compositions included for reference (Ref. 18).

Bead-on-plate welding was conducted by gas metal arc welding (GMAW) perpendicular to the rolling direction of the workpiece. The dimensions of the workpiece were 20 cm long, 10 cm wide, and 9.5 mm thick. It was welded in the length direction in the as-received condition.

The welding parameters were 7.41 mm/s (17.5 in./min) welding speed, 30 V arc voltage, 245 A average current, and Ar shielding. The filler metal was an alloy 4043 wire of 1.2-mm diameter. Its nominal composition is Al-5.2 wt-% Si. The wire feeding speed was 18.6 cm/s (440 in./min).

After welding, the base metal and the PMZ were examined. For optical microscopy, alloys 2024 and 7075 were etched by a solution of 0.5 vol-% HF in water, and alloy 6061 was etched by Keller's reagent. Composition measurements were conducted both in the base metal and PMZ by energy dispersive spectroscopy (EDS) at 15 KV. In order to minimize the possible effect of etching on the accuracy of composition measurements, samples were lightly etched with 10 vol-% phosphoric acid for 15 s. However, light etching made the GBs in the base metal difficult to observe. One 6061 sample was etched with Keller's reagent for 30 s to better reveal the PMZ microstructure in SEM images. All SEM images were taken with backscattered electrons at 15 KV and a 9-mm working distance.

Results and Discussion

Liquation Mechanisms

To help understand liquation in the PMZ, liquation mechanisms for wrought binary aluminum alloys will be discussed first. Three liquation mechanisms are proposed in Fig. 1. The binary phase diagram in Fig. 1A is similar to the Al-rich side of the binary Al-Cu phase diagram. The solid solubility limit refers to the maximum solubility of the solute B in the solid phase α. Alloys 1 and 2 are within and beyond the solid solubility limit, respectively. Alloy 2 is similar to wrought aluminum alloy 2219 (essentially Al-6.3 w-% Cu), which is beyond the maximum solid solubility of 5.65 wt-% Cu. In Alloy 2, Al_xB_y particles are stable up to the eutectic temperature T_E because the alloy is in the two-phase region of $\alpha + Al_xB_y$. In Alloy 1, on the other hand, Al_xB_y particles are stable up to the solvus temperature only. Alloy 1 (an Al-4.5%Cu alloy, for instance) contains no such particles before welding if it is solution heat treated in the α-phase region and quenched (Ref. 19).

Liquation in Alloy 2 is initiated by Mechanism I, as shown in Fig. 1B. The PMZ of Alloy 2 covers the area where the peak temperature during welding is between the liquidus temperature T_{L2} and the eutectic temperature T_E. Upon heating to T_E, liquation begins by the eutectic reaction $Al_xB_y + \alpha \rightarrow L$. Since Al_xB_y is thermodynamically stable up to T_E, liquation occurs at T_E regardless of the heating rate during welding.

Before proceeding further, it is worth mentioning the eutectic reaction at the eu-

tectic temperature here represents the initiation of liquation. Above the eutectic temperature, the eutectic liquid increases in volume and becomes hypoeutectic in composition as the adjacent α matrix dissolves into the liquid. The fraction of the liquid depends on the location in the PMZ. The closer to the fusion boundary, the higher the local peak temperature is and the greater the fraction liquid becomes, as dictated by the phase diagram. At the fusion boundary, the fraction of liquid becomes one. This is true regardless of the mechanism by which liquation is initiated by.

Liquation is initiated in Alloy 1 either by Mechanism II or III, as shown in Fig. 1C. It is by Mechanism II if Al_xB_y particles are present and if the heating rate is high enough to keep Al_xB_y from dissolving completely in α before reaching T_E. The residual Al_xB_y, if there is still any at T_E, will initiate liquation at T_E by the eutectic reaction $Al_xB_y + \alpha \rightarrow L$. The resultant PMZ covers the area where the peak temperature during welding is between the liquidus temperature T_{L1} and the eutectic temperature T_E. Mechanism II is the same as the constitutional liquation mechanism proposed by Pepe and Savage (Refs. 16, 17), which is well recognized in some steels and Ni-based superalloys but not aluminum alloys.

Liquation can also be initiated in Alloy 1 by Mechanism III if no Al_xB_y particles are present at T_E to cause liquation. This happens when Alloy 1 is heated slowly during welding and Al_xB_y particles dissolve in α before reaching T_E or when Alloy 1 is solutionized and quenched before welding (Ref. 19). Liquation occurs by melting of the α phase, $\alpha \rightarrow L$, at the solidus temperature T_{S1} rather than by the eutectic reaction at T_E. Consequently, the resultant PMZ covers the area where the peak temperature during welding is between the liquidus temperature T_{L1} and the solidus temperature T_{S1}.

For wrought ternary aluminum alloys, the three liquation mechanisms shown in Fig. 2 are proposed. These mechanisms correspond to those for wrought binary alloys shown in Fig. 1. In a ternary phase diagram, the solid solubility limit is represented by a nonisothermal curve, while in a binary one, it is represented by a point of fixed composition and temperature (Fig. 1A). Again, Alloy 2 is beyond the solid solubility limit, and particles $Al_xB_yC_z$ can react with the Al-rich phase α to initiate liquation by Mechanism I. Alloy 1 is within the limit, and liquation can be initiated by either Mechanism II or III, depending on whether the liquation-inducing particles $Al_xB_yC_z$ are present at the reaction temperature or not.

According to Hatch (Ref. 20), both alloys 7075 and 6061 are within the solid solubility limit. Therefore, their liquation mechanisms can be expected to be either Mechanism II or III — Fig. 2. Also according to Hatch (Ref. 20), alloy 2024 is near the limit, and it can be either beyond or within the solid solubility limit, depending on the actual composition of the heat. If it is beyond the limit, the liquation mechanism can be expected to be Mechanism I. If it is within the limit, on the other hand, the liquation mechanism can be expected to be either Mechanism II or III.

Multicomponent phase diagrams, if they can be constructed, are rather complicated and difficult to understand. Therefore, it will be convenient if ternary phase diagrams can be used as an approximation to check if an alloy is within or beyond the limit. Figure 3 shows the solid solubility limits in the ternary phase diagrams of Al-Zn-Mg, Al-Si-Mg, and Al-Cu-Mg near the Al corner (Ref. 21). According to the workpiece compositions shown in Table 1, alloy 7075 is close to ternary Al-5.7Zn-2.6Mg by wt-%, which is well within the solid solubility limit as shown in Fig. 3A. Likewise, alloy 6061 is close to ternary Al-0.9Mg-0.6Si by wt-%, which is also within the solid solubility limit as shown in Fig. 3B. Alloy 2024 is close to Al-4.2Cu-1.3Mg by wt-%, which is near the solid solubility limit as shown in Fig. 3C. Therefore, it appears that ternary phase diagrams can be used as an approximation to determine the location of a multicomponent alloy with respect to the solid solubility limit.

Since an alloy is either within or beyond the solid solubility limit, Mechanisms I, II, and III cover the liquation mechanisms in most, if not all, wrought aluminum alloys.

Table 1 — Actual and Nominal (Ref. 18) Compositions (in wt-%) of the Workpiece

	Si	Cu	Mn	Mg	Cr	Zn	Ti	Fe
Alloy 2024								
Actual	0.15	4.18	0.63	1.25	0.01	0.06	0.02	0.24
Nominal	—	4.4	0.6	1.5	—	—	—	
Alloy 7075								
Actual	0.08	1.57	0.03	2.55	0.20	5.7	0.02	0.28
Nominal	—	1.6	—	2.5	0.23	5.6	—	
Alloy 6061								
Actual	0.62	0.28	0.08	0.89	0.19	0.02	0.01	0.52
Nominal	0.6	—	0.28	1.0	0.2	—	—	—

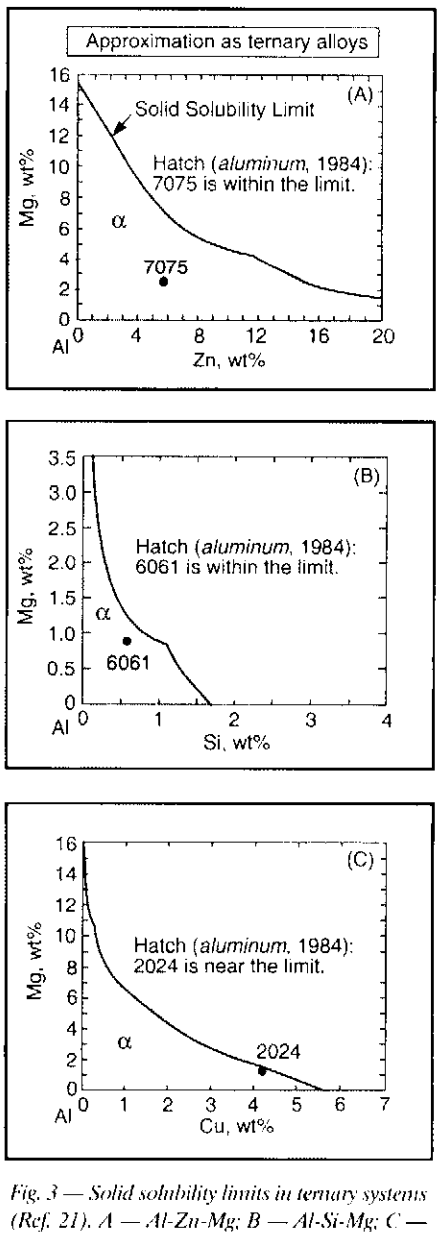

Fig. 3 — Solid solubility limits in ternary systems (Ref. 21). A — Al-Zn-Mg; B — Al-Si-Mg; C — Al-Cu-Mg. As indicated, the approximate locations of alloys 7075, 6061, and 2024 are consistent with the locations according to Hatch (Ref. 20).

Liquation-Inducing Particles and Liquation Reactions

The compositions of the predominant particles in the base metal were determined to help understand the liquation re-

Table 2 — Compositions (in at.-%) of Particles and a Grain Boundary in Alloy 2024

Position	Si	Cu	Mn	Mg	Cr	Zn	Fe	Al
Base Metal (Fig. 4)								
a1	0.04	33.52	0.00	0.32	0.17	0.39	0.33	65.22
a2	0.07	35.81	0.05	0.36	0.04	0.12	0.19	63.35
a3	0.06	34.30	0.02	0.54	0.10	0.05	0.09	64.85
b1	6.33	7.02	5.76	0.00	0.00	0.32	9.45	71.11
b2	6.19	8.66	6.01	0.07	0.01	0.00	10.31	68.75
b3	5.91	5.94	6.95	0.10	0.16	0.31	10.65	69.98
Partially Melted Zone (Fig. 8A)								
p1	6.56	5.80	4.95	0.00	0.05	0.08	9.81	72.75
p2	6.74	2.77	6.98	0.00	0.08	0.10	7.99	75.34
p3	0.62	23.60	0.08	8.36	0.02	0.00	0.12	67.20
g1	2.64	15.14	0.02	2.26	0.05	0.00	0.00	79.88

actions in each alloy. Compositions of similar particles at different locations were compared to check the consistency of EDS analyses. Iron-rich particles existed in the base metal of each alloy. Iron (Fe) is an ever-present impurity in Al and particles form because the solubility of Fe in solid Al is very low.

Alloy 2024

The EDS results for the particles in the base metal (and the PMZ) of alloy 2024 are listed in Table 2 in at.-%. Referring to Fig. 4, the compositions (in at.-%) of the particles in the base metal were essentially:

Cu-rich particles

Al-34Cu at *a1*, Al-36Cu at *a2*, and Al-34Cu at *a3*

Fe-rich particles

Al-9Fe-7Cu-6Si-6Mn at *b1*,
Al-10Fe-9Cu-6Si-6Mn at *b2*, and
Al-11Fe-7Mn-6Si-6Cu at *b3*.

The Cu-rich particles appeared to be $CuAl_2$ (that is, Al-33Cu in at.-%). $CuAl_2$ (and $CuMgAl_2$) particles have been observed in alloys 2219, 2024, and 2014

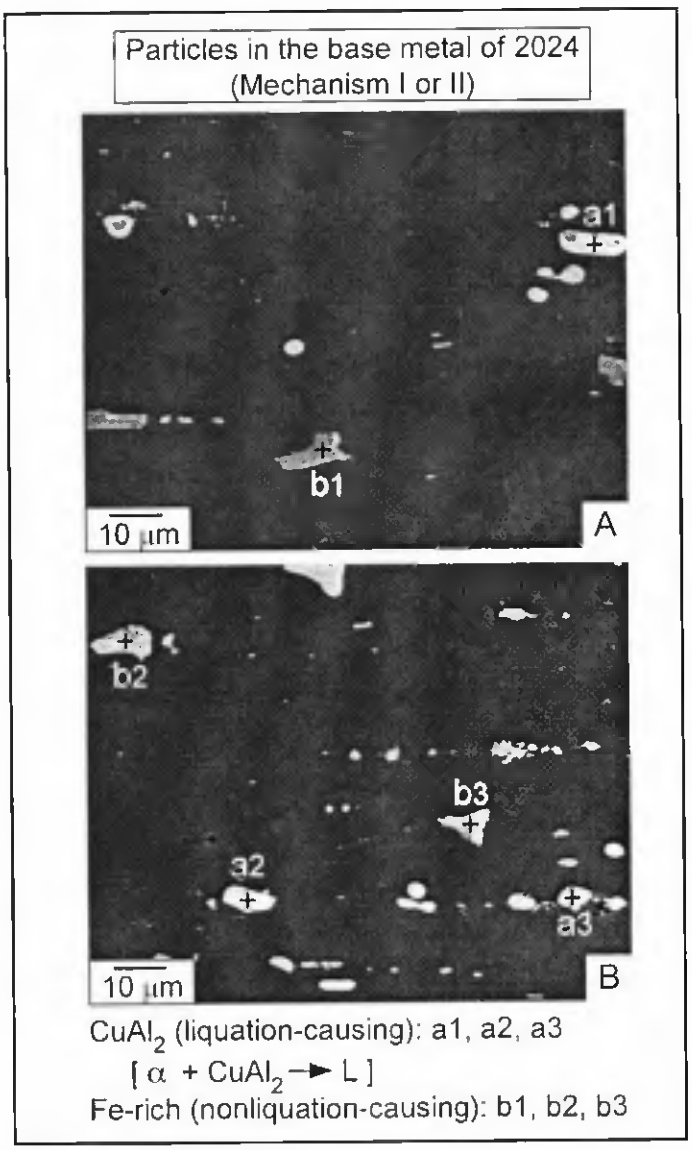

Fig. 4 — SEM images of alloy 2024 at two different locations in the base metal.

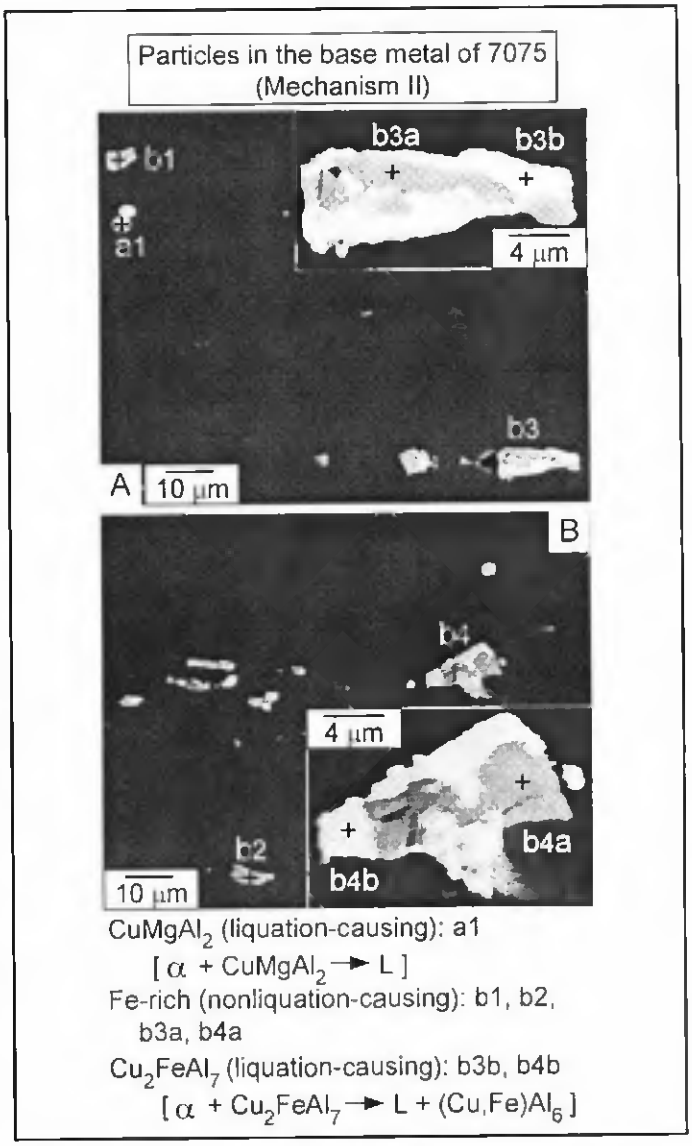

Fig. 5 — SEM images of alloy 7075 at two different locations in the base metal.

(Refs. 13, 14, 20, 22, 23). $CuAl_2$ particles can cause liquation by the following eutectic reaction (Ref. 23):

$$\alpha + CuAl_2 \rightarrow L \text{ at } 548°C. \quad (1)$$

Above the eutectic temperature the surrounding Al matrix melts into the eutectic liquid and dilutes it to a hypoeutectic liquid. Upon subsequent cooling, the hypoeutectic liquid solidified first as α and last as eutectic ($\alpha + CuAl_2$). Small $CuAl_2$ particles were present along the GBs in the base metal (though too small for composition analysis) and they can cause GB liquation, as observed in alloy 2219 (Ref. 13).

The presence of many large $CuAl_2$ particles in the base metal and a composition near the solid solubility limit together suggested the as-received alloy 2024 was either beyond the solid solubility limit or was within the limit but had not been solution heat-treated thoroughly to dissolve $CuAl_2$. In the former case, Mechanism I can occur regardless of the heating rate during welding. In the latter, however, Mechanism II (constitutional liquation) can occur under rapid heating. $CuMgAl_2$ particles, though not shown in Fig. 4, are likely to be present to cause similar liquation (Reaction 2).

The Fe-rich particles were similar to those insoluble by heat treating. Examples of such particles include $(Fe,Cu,Mn)_3SiAl_{12}$ (19 at.-% for Fe, Cu, and Mn together, and 6 at.-% for Si alone) or $(Fe,Cu,Mn)_3Si_2Al_{15}$ (15 at.-% for Fe, Cu, and Mn together, and 10 at.-% for Si alone) (Refs. 20, 22, 23). No liquation-causing reactions between Fe-rich particles and the Al matrix were found in the numerous reactions listed by Mondolfo (Ref. 23).

Alloy 7075

The EDS results for the particles in the base metal (and the PMZ) of alloy 7075 are listed in Table 3 in at.-%. Referring to Fig. 5, the compositions (in at.-%) of the particles in the base metal were

Cu-rich particles

Al-26Cu-23Mg at *a1*

Fe-rich particles

Al-14Fe-4Cu-2Zn at *b1*,
Al-13Fe-4Cu-2Zn at *b2*,
Al-15Fe-4Cu-2Zn at *b3a*, and
Al-14Fe-4Cu-2Zn at *b4a*,

Cu-rich coatings

Al-19Cu-9Fe at *b3*b and
Al-21Cu-10Fe at *b4b*.

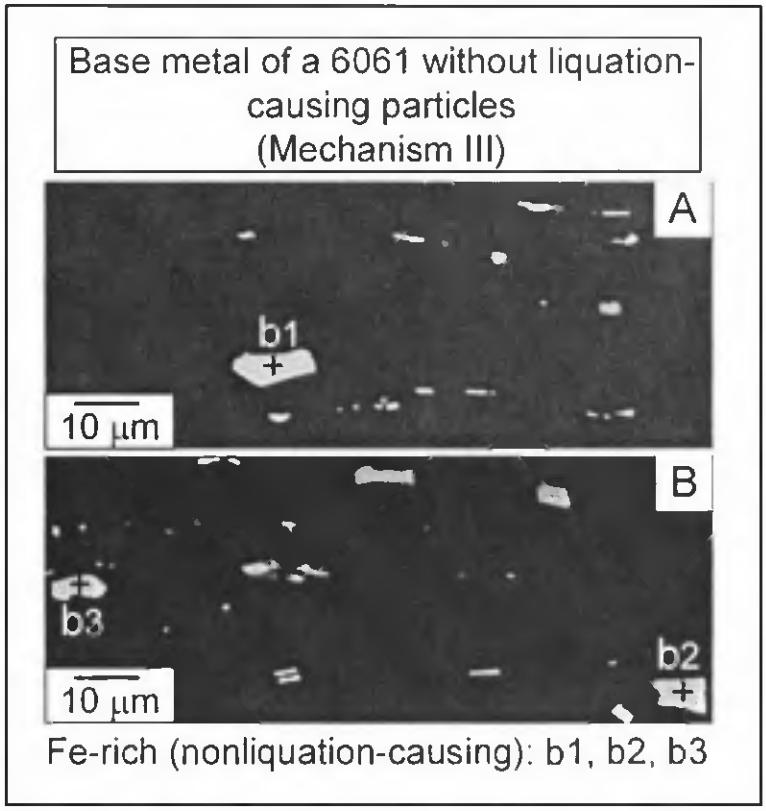

Fig. 6 — SEM images of alloy 6061 at two different locations in the base metal.

Table 3 — Compositions (in at.-%) of Particles and a Grain Boundary in Alloy 7075

Position	Si	Cu	Mn	Mg	Cr	Zn	Fe	Al
				Base Metal (Fig. 5)				
a1	0.03	26.08	0.00	22.99	0.07	1.86	0.16	48.81
b1	0.00	4.38	0.37	0.13	0.17	1.97	13.68	79.30
b2	0.00	3.78	0.40	0.28	0.25	2.19	13.16	79.94
b3a	0.00	4.28	0.24	0.19	0.25	2.27	14.58	78.19
b4a	0.71	3.96	0.47	0.06	0.15	1.88	14.31	78.47
b3b	0.00	18.87	0.11	0.23	0.26	0.84	9.04	70.65
b4b	0.50	20.77	0.13	0.14	0.17	0.56	9.81	67.91
				Partially Melted Zone (Fig. 8B)				
p1	0.00	3.16	0.39	0.09	0.18	1.77	14.57	79.85
p2	0.11	9.51	0.03	14.54	0.04	11.82	0.00	63.95
p3a	0.48	3.77	0.67	1.65	1.89	2.90	11.88	76.76
p3b	0.00	9.28	0.01	15.48	0.04	13.30	0.07	61.82
g1	0.00	6.75	0.09	12.07	0.44	9.45	0.00	71.20

Table 4 — Compositions (in at.-%) of Particles and a Grain Boundary in Alloy 6061

Position	Si	Cu	Mn	Mg	Cr	Zn	Fe	Al
				Base Metal (Fig. 6)				
b1	8.26	0.75	1.00	0.02	1.70	0.00	15.53	72.74
b2	7.85	0.82	0.84	0.00	1.25	0.18	16.48	72.58
b3	8.60	0.58	1.04	0.01	2.49	0.02	14.77	72.50
				Partially Melted Zone (Fig. 8C)				
p1	8.21	1.39	0.79	0.09	1.97	0.00	15.70	71.85
p2	5.66	1.00	1.12	0.11	1.82	0.00	17.46	72.83
g1	19.68	3.88	0.00	9.96	0.04	0.00	0.14	66.30

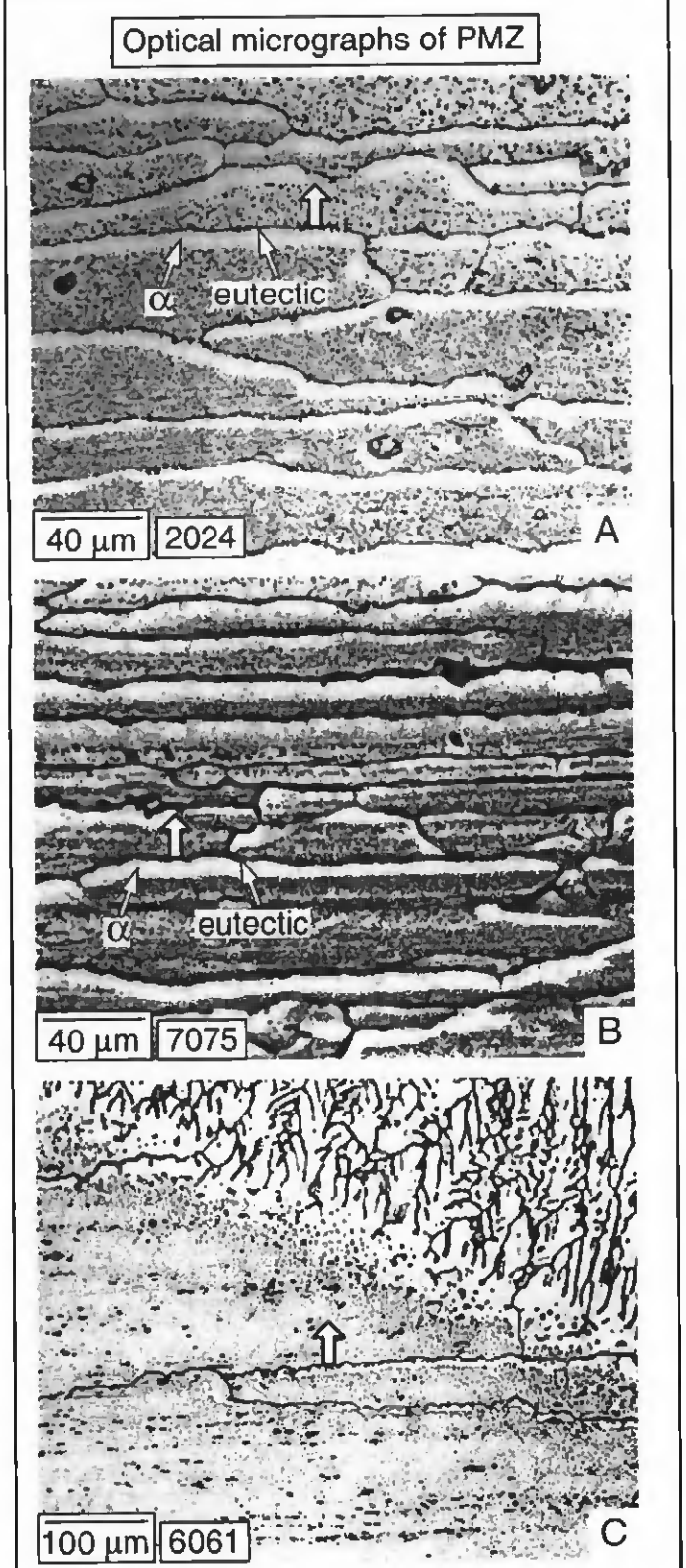

Fig. 7 — Optical micrographs of the partially melted zone. A — Alloy 2024; B — alloy 7075; C — alloy 6061.

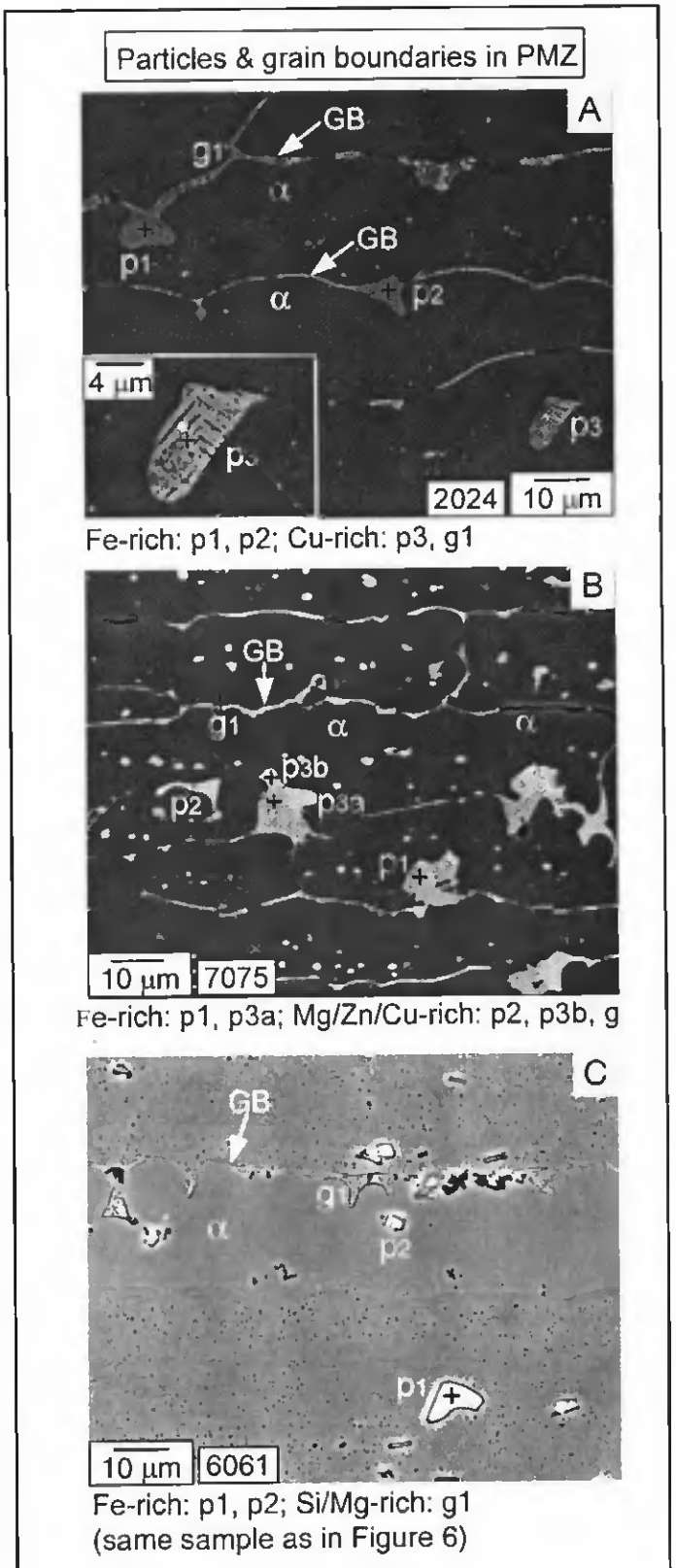

Fig. 8 — SEM images of the partially melted zone. A — Alloy 2024; B — alloy 7075; C — alloy 6061 in Fig. 6. In alloy 6061, the thick grain boundary liquid and the little grain interior liquid suggest the liquid from the weld pool penetrated deep into the partially melted zone along the grain boundary.

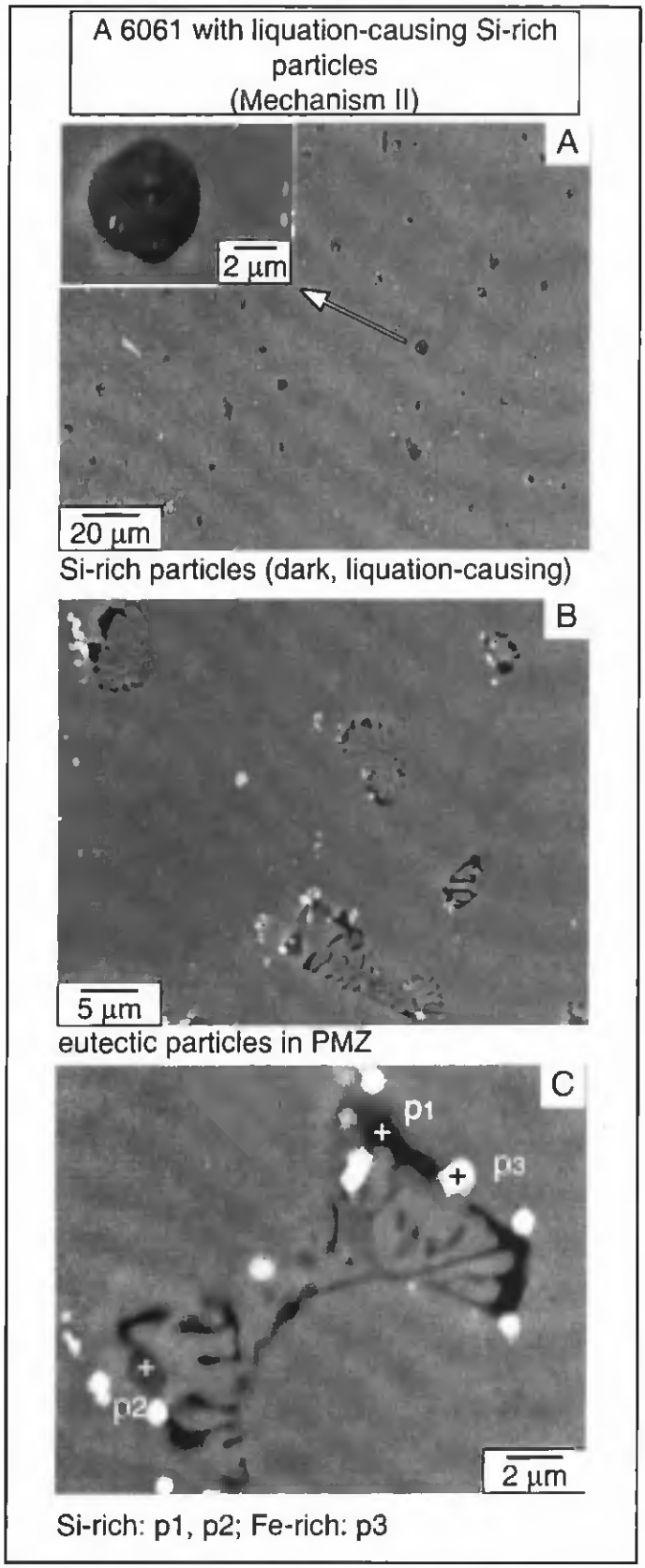

Fig. 9 — SEM images of an alloy 6061 from a second supplier. A — Dark liquation-causing Si-rich particles in base metal; B — eutectic particles in PMZ; C — eutectic particle in PMZ enlarged.

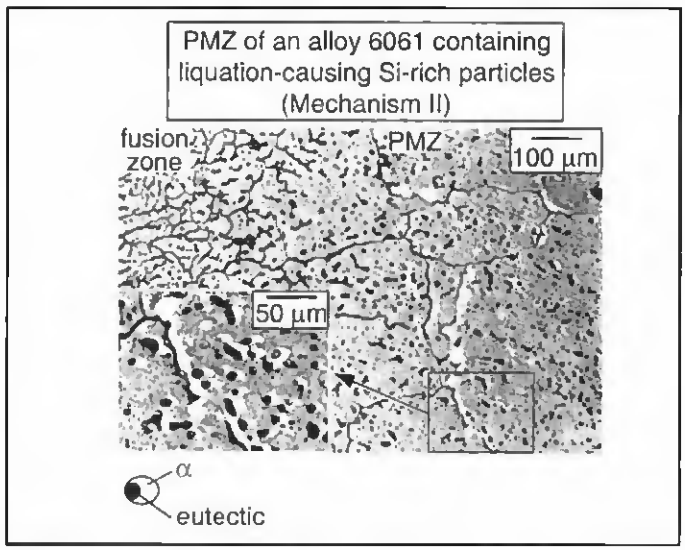

Fig. 10 — PMZ optical micrograph of the alloy 6061 in Fig. 9 showing eutectic particles resulting from liquation caused by Si-rich particles.

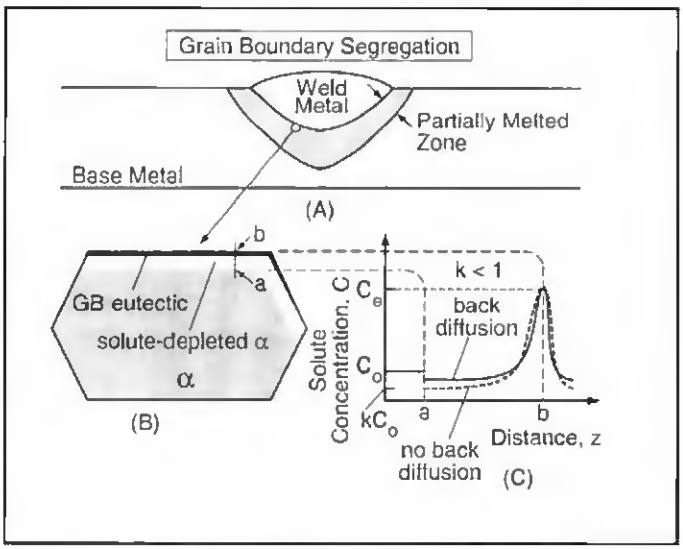

Fig. 11 — Grain boundary segregation in the partially melted zone.

The Cu-rich particles appeared to be $CuMgAl_2$ (that is, Al-25Cu-25Mg in at.-%) (Refs. 20, 23). The presence of some $CuMgAl_2$ particles in the base metal suggested the solution heat treatment of the as-received alloy 7075 was not thorough enough. $CuMgAl_2$ particles can cause liquation by the following eutectic reaction (Ref. 23):

$$\alpha + CuMgAl_2 \rightarrow L \text{ at } 518°C. \quad (2)$$

As shown in Fig. 3A, alloy 7075 is considered an Al-Zn-Mg ternary alloy just for determining the approximate location of the alloy relative to the solid solubility limit. This does not contradict the presence of Cu-rich particles or coatings in the alloy.

These Fe-rich particles (in Fig. 5) differed from those in the base metal of alloy 2024 (Fig. 4) because they had some Zn but little Si and Mn due to the composition of alloy 7075. Liquation-causing reactions between such Fe-rich particles and the Al matrix were not found (Ref. 23).

The Cu-rich coatings appeared to be Cu_2FeAl_7 (that is, Al-20Cu-10Fe in at.-%)

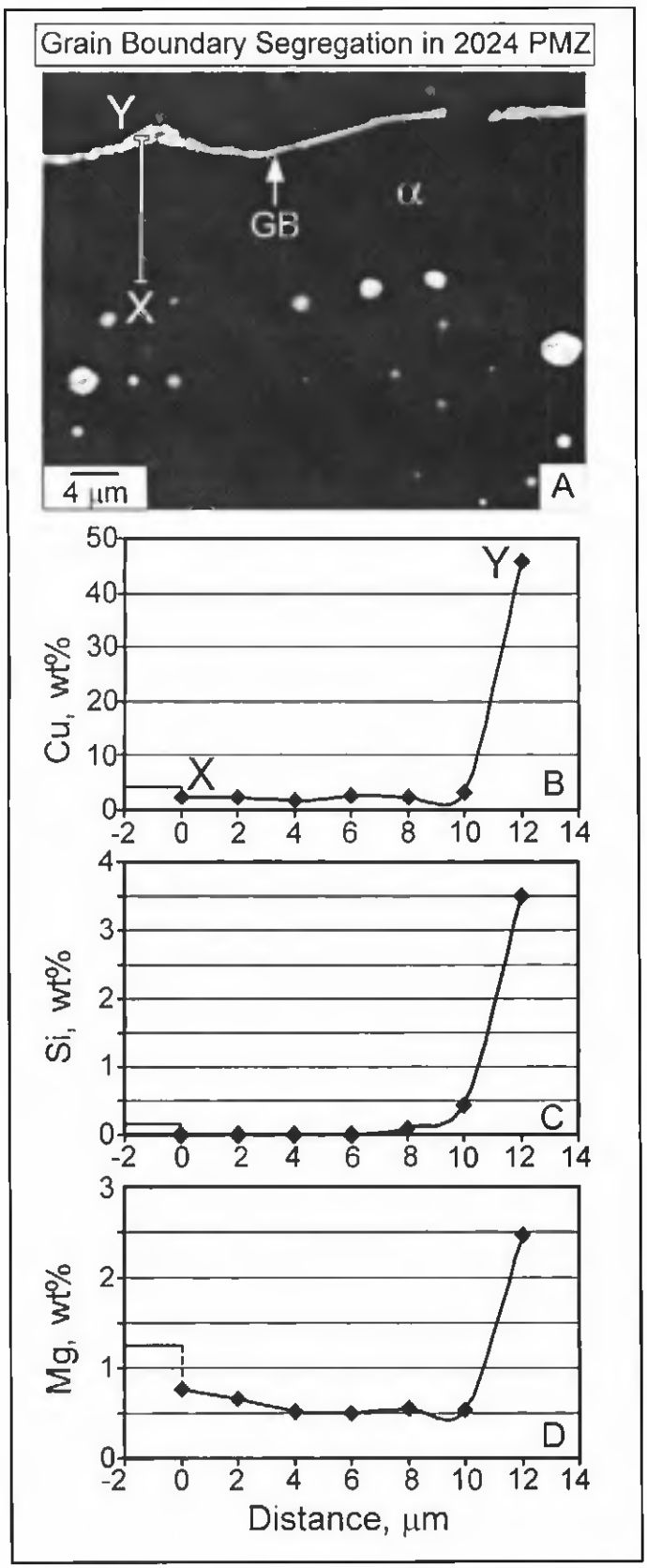

Fig. 12 — Grain boundary segregation in the partially melted zone of alloy 2024. A — SEM image; B — Cu; C — Si; D — Mg. The overall composition of the workpiece (Table 1) is included for reference (from –2 to 0 μm).

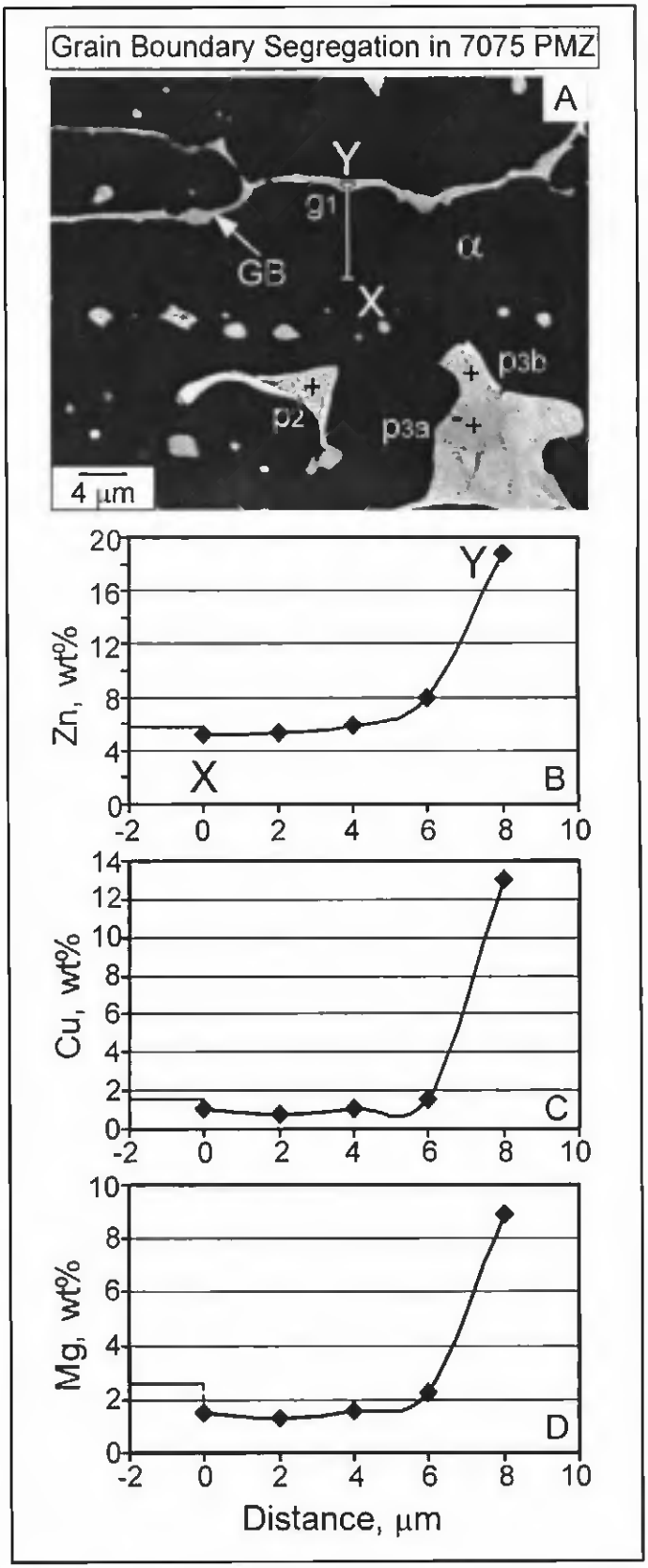

Fig. 13 — Grain boundary segregation in the partially melted zone of alloy 7075. A — SEM image; B — Zn; C — Cu; D — Mg.

(Refs. 20, 23). Fe-rich particles are known to transform to Cu_2FeAl_7 during heat treating of alloy 7075 ingots (Ref. 20). The following reaction is known to exist (Ref. 23):

$$\alpha + Cu_2FeAl_7 \rightarrow L + (Cu,Fe)Al_6 \text{ at } 590°C. \quad (3)$$

Therefore, Cu_2FeAl_7 on the surface of Fe-rich particles was likely to cause liquation by reacting with the surrounding Al matrix.

Alloy 6061

The EDS results for the particles in the base metal (and the PMZ) of alloy 6061 are listed in Table 4 in at.-%. Referring to Fig. 6, the compositions (in at.-%) of the particles in the base metal were essentially:

Fe-rich particles

Al-16Fe-8Si-2Cr-1Mn at *b1*,
Al-16Fe-8Si-1Cr-1Mn at *b2*, and
Al-15Fe-9Si-2Cr-1Mn at *b3*.

The Fe-rich particles were often thin and, when oriented normal to the polishing surface, appear as short line segments. Liquation-causing reactions between such Fe-rich particles and the Al matrix were not found (Ref. 23).

No liquation-causing particles were found in this alloy 6061. Since the Fe-rich particles did not caused liquation and there were no liquation-causing particles present, liquation occurred by Mechanism III in this alloy 6061.

However, coarse Mg_2Si particles were reported to be present and cause liquation in alloy 6061 (Refs. 20, 22, 23). To resolve this discrepancy, an alloy 6061 from a different supplier was also welded, as will be discussed later.

PMZ Microstructure

The PMZ optical micrographs are shown in Fig. 7. As shown, the liquated and resolidified GB material consisted of a light etching α band that solidified first and a dark etching eutectic GB that solidified last. GB solidification was directional, that is, upward (indicated by the thick arrows) and toward the weld (Ref. 13). The latter was clearer in alloy 2024 because of more GBs facing the weld (to the upper right of the micrograph). The SEM images of the PMZ are shown in Figure 8. It is interesting to note the α band appeared as dark etching while the eutectic GB appeared as light etching.

Alloy 2024

The EDS results for the particles in the PMZ of alloy 2024 are listed in Table 2 in at.-%. Referring to Fig. 8A, the compositions (in at.-%) of the particles were essentially:

Fe-rich particles

Al-10Fe-7Si-6Cu-5Mn at *p1* and
Al-8Fe-7Si-7Mn-3Cu at *p2*

Cu-rich particle

Al-24Cu-8Mg-1Si at *p3*

Grain boundary

Al-15Cu-3Si-2Mg at *g1*.

The compositions of Fe-rich particles were close to those of the Fe-rich particles at *b1* through *b3* in the base metal — Fig. 4. As evident in SEM images of higher magnifications (not shown here because of space limitations), these Fe-rich particles looked similar in microstructure to the Fe-rich particles in the base metal.

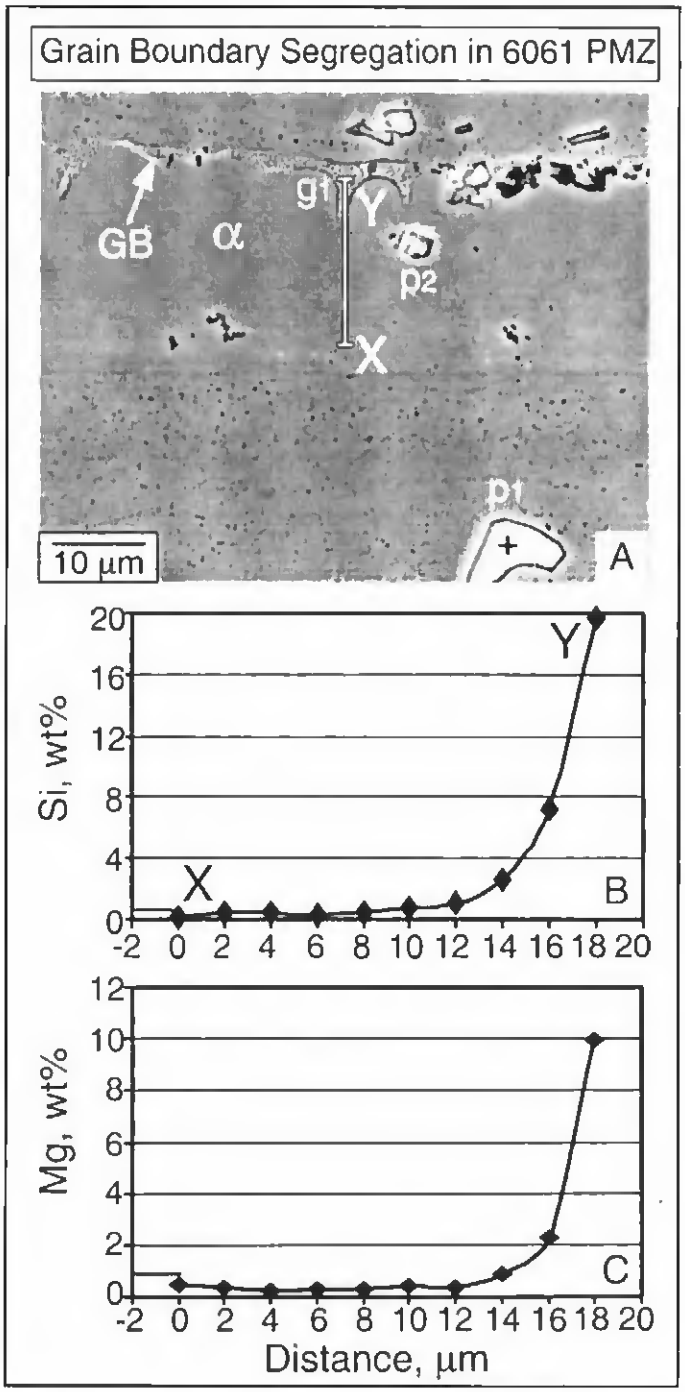

Fig. 14 — Grain boundary segregation in the partially melted zone of the alloy 6061 in Fig. 6. A — SEM image; B — Si; C — Mg.

Therefore, it appeared Fe-rich particles did not react with the Al matrix to cause liquation. Otherwise, their composition and microstructure would have changed.

The Cu-rich particle at *p3* had a composite-like structure of a normal eutectic and a particle-free α ring surrounding it as shown in the inserted micrograph in Fig. 8A. It appeared a large $CuAl_2$ particle reacted with the Al matrix and caused liquation here, and the eutectic particle formed during subsequent solidification. Since the Al matrix contained Mg (Table 1), it brought Mg into the liquid hence the resultant eutectic particle at *p3*. It was also possible some $CuMgAl_2$ particles were present in the base metal, and they reacted with the Al matrix to cause liquation and formed the particle at position *p3* upon solidification.

The GB at *g1* had a composite-like eutectic structure, as evident from SEM images of higher magnifications (not shown), and it had a particle-free α band below it. These were typical signs of a liquated GB (Refs. 13–15). Its Cu and Mg contents were lower than those of the eutectic particle at *p3*, possibly because the GB was relatively thin and the electron beam in EDS included the surrounding Al matrix of lower Cu and Mg contents.

Alloy 7075

The EDS results for the particles in the PMZ of alloy 7075 are listed in Table 3 in at.-%. Referring to Fig. 8B, the compositions (in at.-%) of the particles and grain boundary were essentially:

Fe-rich particles

Al-15Fe-3Cu-2Zn at *p1*,
Al-12Fe-4Cu-3Zn-2Cr-2Mg at *p3a*

Mg,Zn,Cu-rich particles

Al-15Mg-12Zn-10Cu at *p2*,
Al-15Mg-13Zn-9Cu at *p3b*, and

Grain boundary

Al-12Mg-9Zn-7Cu at *g1*.

The composition of the particle at *p1* was close to those of the Fe-rich particles in the base metal (*b1* and *b2* in Fig. 5). This particle was, therefore, a bare Fe-rich particle that did not dissolve.

The particle at *p2* had a composite-like structure of a normal eutectic (shown later in Fig. 13A at a higher magnification). The eutectic reaction involving a eutectic liquid of this composition was not found (Ref. 23). The high Mg and Cu contents of this particle suggested it was likely a large $CuMgAl_2$ particle liquated here, incorporated Zn from the surrounding matrix, and solidified into a eutectic particle rich in Mg, Zn, and Cu.

The GB at *g1* has a composite-like structure (as observed under higher magnifications) and a Mg/Zn/Cu-rich composition like the particle at *p2*. Its Mg, Zn, and Cu contents appeared lower than those of the particle at *p2*, possibly because of the background effect of this thin GB in the EDS composition analysis.

Consider the particle at position, *p3*, which was labeled at two positions, *p3a* and *p3b* (shown later in Fig. 13A at a higher magnification). It was interesting to note the liquated material at *p3* (its lower left corner) penetrated into the GB. It was also interesting to note the particle at position *p3* was on the average brighter on the outside and somewhat darker inside. This particle is discussed further as follows.

As mentioned previously, the base metal contained Fe-rich particles with Cu_2FeAl_7 on the surface. One possibility was Cu_2FeAl_7 liquated but the Fe-rich portion did not dissolve in the liquid produced by the liquation process. However, the material at position *p3b* was essentially Al-15Mg-13Zn-9Cu by at.-% and contained little Fe. This suggested it did not come from the liquation of Cu_2FeAl_7. Furthermore, the material at position *p3a* was essentially Al-12Fe-4Cu-3Zn-2Cr-2Mg by at.-% and had more Cr and less Fe than those at positions *b3a* and *b4a* in Fig. 5. This suggested it did not come from the undissolved Fe-rich portion of a particle like *b3* and *b4* in the base metal.

The other possibility was that Cu_2FeAl_7 liquated, for instance, through Reaction 3 and formed $(Cu,Fe)Al_6$. As the temperature rose further, the volume of liquid increased by melting the surrounding Al matrix and $(Cu,Fe)Al_6$. During subsequent solidification of the resultant liquid, the Fe-rich portion of the particle at *p3* formed first and then the Cu-containing portion. It was interesting to note the composition of the material at *p3b* was close to that of the normal eutectic at position *p2*. It is possible the Fe-rich solid precipitated from the liquid and grew and became the Fe-rich portion and, upon further cooling, the eutectic nucleated heterogeneously on the Fe-rich portion and formed the Cu-containing portion.

Alloy 6061

The EDS results for the particles in the PMZ of alloy 6061 are listed in Table 4 in at.-%. Referring to Fig. 8C, the compositions of the particles (in at.-%) and grain boundary were essentially:

Fe-rich particles

Al-16Fe-8Si-2Cr-1Mn-1Cu at *p1*,
Al-17Fe-6Si-2Cr-1Mn-1Cu at *p2*

Grain boundary

Al-20Si-10Mg-4Cu at *g1*.

The sample in Fig. 8C was etched with Keller's regent for 30 s to reveal the PMZ microstructure more clearly in the SEM image. Otherwise, only Fe-rich particles would have been visible (Fig. 6). As shown previously, the base metal of alloy 6061 contained angular Fe-rich particles (Fig. 6) but no liquation-causing reactions between these Fe-rich particles and the Al matrix were found (Ref. 23). Figure 8C is further discussed as follows.

The composition of the particle at *p1* was similar to the compositions of the Fe-rich particles in the base metal (*b1* through *b3* in Fig. 6). Its microstructure was also similar to that of the Fe-rich particles, that is, without a composite-like eutectic. The groove around the particle was caused by etching. These similarities suggested Fe-rich particles do not cause liquation in alloy 6061. The small particle at *p2* was a similar Fe-rich particle that happened to be close to the GB, and was caught in the GB liquid.

The GB at *g1* had a composite-like structure of a normal eutectic and a particle-free α band below it, typical of a liquated GB.

It was interesting to note in Fig. 8 that the amount of liquid along one GB was much greater in alloy 6061 than in alloy 2024 or 7075, even though alloy 6061 was much less alloyed and thus can be expected to liquate less. It was not likely liquation alone could produce so much GB liquid in alloy 6061, especially when there was little liquation in the grain interior. Therefore, most of the GB liquid could have come from the weld pool.

As mentioned previously, coarse Mg_2Si particles were reported to be present in alloy 6061 (Refs. 20, 22, 23), and Al-Mg_2Si eutectic particles were reported to be present in the PMZ of such an alloy 6061 (Ref. 22). However, no coarse Mg_2Si particles were observed in the 6061 base metal in Fig. 6, and no Al-Mg_2Si eutectic particles were observed in the 6061 PMZ in Fig. 8C, either.

To resolve the discrepancy between the present study and previous studies regarding the presence of coarse Mg_2Si particles in alloy 6061, additional welding experiments were conducted on similar 6061 plates from a supplier different from that of the alloy 6061 shown in Fig. 6. Figure 9A shows the SEM image of the base metal of a 6061-T651 plate from one such supplier. Unlike the alloy 6061 shown in Fig. 6, many dark particles were present in the base metal. One such particle was enlarged for closer examination. The sample was not etched at all in order not to dis-

solve the dark particles, which disappeared quickly even just briefly etched. Results of EDS analysis showed these particles had different compositions. Examples of the compositions (in at.-%) included Al-47Si-1Cu (the dark particle shown in the enlarged SEM image in Fig. 9A), Al-41Si-1Fe, Al-34Si, Al-49Si-20Mg-3Cu, Al-41Si-14Mg-5Cu-3Zn, Al-36Si-22Zn-1Mg, and Al-29Si-19Zn-1Cu. As such, these dark particles in the base metal were Si-rich particles with various concentrations of Mg, Cu, and Zn. These particles may have come from the eutectic particles formed during the terminal stage of casting. However, since alloy 6061 is within the solid solubility limit, the presence of the Si-rich particles in the base metal suggests the solution heat treatment was not thorough enough to dissolve these particles completely. Most of these particles looked similar to that shown in the enlarged SEM image in Fig. 9A. They did not look like composites but had some light Fe/Cu-rich particles embedded in them. Apparently, these dark, Si-rich particles were much more complicated in composition and had less Mg than the previously reported Mg_2Si particles (Refs. 20, 22, 23). No composition analysis was shown to back up the claim of Mg_2Si. As shown in Fig. 9A, there appeared to be some light angular Fe-rich particles scattered in the base metal as well.

In the PMZ these dark, Si-rich particles caused liquation by reacting with the surrounding Al matrix and formed eutectic particles, such as those shown in Figs. 9B and 9C. Results of EDS analysis showed that the dark areas in the eutectic were mostly Si-rich with various concentrations (in at.-%) of Mg, Cu, Zn, and Fe, for instance, Al-38Si-10Mg-5Cu (*p1* in Fig. 9C), Al-20Si-8Zn-4Mg-3Cu, Al-12Si-4Mg-4Fe-3Cu, Al-29Mg-16Si-7Zn-2Cu (*p2* in Fig. 9C), and Al-18Zn-16Si-3Cu. The light spots in the eutectic, on the other hand, were Fe-rich particles with Cu, Mg, Zn, and Si, for instance, Al-18Fe-12Cu-6Zn-3Si (*p3* in Fig. 9C), and Al-15Fe-9Cu-8Mg-4Si-3Zn. Apparently these eutectic particles had more complicated compositions than the Al-Mg_2Si eutectic composition previously reported (Ref. 22). No EDS results were shown to substantiate the claim of the Al-Mg_2Si eutectic composition.

Figure 10 shows an optical micrograph of the PMZ in this 6061 plate. A portion of the PMZ was enlarged for clarity. As shown, a light etching α phase surrounds the dark etching eutectic particle. The dark etching eutectic particles are the eutectic particles shown previously in Fig. 9B, though the light etching α phase was not light under SEM. This is clear evidence of liquation caused by dark particles in the base metal shown in Fig. 9A. In the PMZ of alloy 2219, a light etching α phase surrounds the dark etching eutectic particle of Al-$CuAl_2$ as a result of liquation caused by coarse $CuAl_2$ particles (Refs. 13–15). The α phase is light in optical micrographs, but not the SEM images.

According to the compositions of the dark, Si-rich particles in the matrix, they can cause liquation by the following and other eutectic reactions (Ref. 23):

$$\alpha + Si \rightarrow L \text{ at } 577°C \quad (4)$$

$$\alpha + Mg_2Si + Si \rightarrow L \text{ at } 555°C \quad (5)$$

Grain Boundary Segregation

Figure 11 provides a mechanism for the GB segregation that develops during solidification of the GB liquid in the PMZ. Allowing C_0 to be the concentration of a given alloying element in the base metal, theoretically, the concentration of the GB eutectic, C_e, is the composition of the eutectic if the GB eutectic is normal, and of Al_xB_y if the GB eutectic is divorced. In practice, the value of C_e can be affected by the GB thickness if it is not significantly greater than the interaction volume of electrons in the EDS analysis. In the absence of solute back diffusion into the solidified material, the concentration of the element at the starting edge of the α band should be kC_0, where k is the equilibrium partition ratio of the element. The dash line shows the resultant GB segregation of the element. However, if back diffusion is significant, the concentration of the element at the starting edge of the α band will be greater than kC_0, as the solid line indicates.

In the case of alloy 2219 (Al-6.3 wt-% Cu with k = 0.17), back diffusion was evident. The Cu concentration at the starting edge of the α strip was essentially 3 wt-%, which was significantly higher than the 1.07 wt-% Cu based on kC_0 (= 0.17 x 6.3 wt-%) (Ref. 14). For the aluminum alloys studied here, back diffusion of alloying elements is expected to be significant. However, this cannot be verified because k is not readily available in multicomponent alloys.

The SEM micrograph in Fig. 12A shows an α band in the PMZ of alloy 2024 and path XY along which solute segregation (in wt-%) across the α band was measured. As shown in Fig. 12 B through D, Cu, Si, and Mg segregated to the GB and the α band became depleted in these elements. For reference, the workpiece composition taken from Table 1 was superimposed on the segregation curve from –2 to 0 μm. As compared to the GB at *g1* in Fig. 8A, this GB had much more Cu and a different microstructure. It should be pointed out that in the PMZ, the GB composition can vary from GB to GB or even within one GB. It can be affected by a large particle nearby (such a Cu-rich particle) if the particle liquates and joins the local GB liquid.

Figure 13 shows GB segregation in the PMZ of alloy 7075. As shown, Zn, Cu, and Mg all segregated heavily to the GB, leaving the α band solute depleted. GB segregation in the PMZ of alloy 6061 in Fig. 6 is shown in Fig. 14. Segregation of Si and Mg to the GB was clear. Like all other liquated GBs in alloy 6061, this GB was connected to the fusion boundary. The location of the segregation measurement is 205 μm from the fusion boundary. It is interesting to note that along the same GB but at 568 μm away from the fusion boundary, the measured segregation shows Si rose from below 1 wt-% in the α band to 25 wt-% at the GB, and Mg rose from below 1 to 1.6 wt-%. As such, much more Si than Mg was present here, even though alloy 6061 had more Mg than Si (Table 1). Based on the diffusion distance d = 568 μm, a typical diffusion coefficient of D = 5 x 10^{-5} cm^2/s in the liquid and the approximation of $d^2 = Dt$, the required time for Si to diffuse from the fusion boundary to this location was t = 65 s. This long diffusion time suggests the high Si content here is not likely to be caused by Si diffusion from the weld pool. Therefore, it appeared the Si-rich liquid from the weld pool backfilled the GB. The liquid was enriched in Si because of the 4043 filler metal (Al-5.2 wt-% Si).

Summary and Conclusions

In summary, since liquation can cause hot cracking and/or severe loss of strength and ductility and since most aluminum alloys are multicomponent, a fundamental study was conducted on the mechanisms by which liquation is initiated in the PMZ of wrought multicomponent aluminum alloys during welding. Three representative liquation-susceptible alloys 2024, 6061, and 7075 were studied. Three liquation mechanisms were identified. The compositions and morphologies of the particles in the base metal were examined in order to help identify the liquation-inducing particles and the corresponding liquation reactions. The compositions and morphologies of both the particles and grain boundary phases in the PMZ were also examined to help further understand the liquation mechanisms. Liquation-induced grain boundary segregation was determined.

Conclusions are as follows:

1) Three different liquation mechanisms have been identified, and they cover most, if not all, of the wrought multicomponent aluminum alloys. For alloys

beyond the solid solubility limit, liquation-inducing particles react with the α matrix and liquation can occur at any heating rate (Mechanism I). For alloys within the limit but with such particles, liquation requires high heating rates (Mechanism II). For alloys within the limit and without such particles, liquation occurs when the aluminum matrix starts to melt (Mechanism III).

2) For a given alloy and temper, for instance, alloy 6061-T651 and alloy 2024-T351, the liquation mechanism can vary from heat to heat, depending on the exact alloy composition and the heat treatment history.

3) Alloy 2024 contains $CuAl_2$ and likely $CuMgAl_2$ particles and is near the solid solubility limit. Therefore, the liquation mechanism depends on the composition of the heat welded. An alloy 2024 can liquate by Mechanism I if it is beyond the solid solubility limit and by Mechanism II if within the limit. In either case, liquation can occur by the following reactions:

$\alpha + CuAl_2 \rightarrow L$ at 548°C, and
$\alpha + CuMgAl_2 \rightarrow L$ at 548°C.

4) Alloy 7075 contains both $CuMgAl_2$ particles and Fe-rich particles coated with Cu_2FeAl_7. It is well within the solid solubility limit and thus liquates by Mechanism II. Liquation can occur by the following reactions:

$\alpha + CuMgAl_2 \rightarrow L$ at 518°C,
$\alpha + Cu_2FeAl_7 \rightarrow L + (Cu,Fe)Al_6$ at 590°C.

5) Alloy 6061 is also within the solid solubility limit. Depending on how thorough the solution heat treatment, it may or may not contain Si-rich particles. Liquation is initiated by Mechanism III when Fe-rich particles alone are present, and by Mechanism II when Si-rich particles are also present. Si-rich particles can cause liquation through, for example, the following reactions:

$\alpha + Si \rightarrow L$ at 577°C

$\alpha + Mg_2Si + Si \rightarrow L$ at 555°C.

6) Ternary phase diagrams can be a useful approximation for determining the location of a multicomponent alloy with respect to the solid solubility limit, at least in the cases of alloys 2024, 6061, and 7075.

7) The liquation-causing particles in alloy 6061, at least in the one studied here, are not Mg_2Si particles as suggested in the literature but Si-rich particles with varying Mg, Cu, and Zn contents. The eutectic particles in the PMZ are not the Al-Mg_2Si eutectic particles as suggested in the literature either, but eutectic particles consisting of Si-rich and Fe-rich phases.

8) Numerous bare Fe-rich particles are present in wrought aluminum alloys, but they do not appear to cause liquation.

9) GB segregation can be rather severe in the PMZ of multicomponent aluminum alloys. Severe GB segregation can dramatically degrade the PMZ mechanical properties, as demonstrated in binary alloy 2219.

Acknowledgments

The authors thank the National Science Foundation (Grant Numbers DMR-9803589 and -0098776) for financial support and Miller Electric Manufacturing Co., Appleton, Wis. for donating the welding equipment used in the present study.

References

1. Kou, S. 1987. *Welding Metallurgy*, pp. 29–59, 239–262. New York, N.Y.: John Wiley and Sons.

2. Arthur, J. B. 1955. Fusion welding of 24S-T3 aluminum alloy. *Welding Journal* 34(11): 558-s to 569-s.

3. Collins, F. R. 1962. Improved strengths in welded high-strength, heat treatable aluminum alloys. *Welding Journal* 41(8): 337-s to 345-s.

4. Schillinger, D. E., Betz, I. G., Hussey, F. W., and Markus, H. 1963. Improved weld strength in 2000 series aluminum alloys. *Welding Journal* 42(6): 269-s to 275-s.

5. Fish, R. F., and Shira, C. S. 1966. Effects of high-frequency current in welding aluminum alloy 6061. *Welding Journal* 45(11): 490-s to 496-s.

6. Dudas, J. H., and Collins, F. R. 1966. Preventing weld cracks in high-strength aluminum alloys. *Welding Journal* 456: 241-s to 249-s.

7. Metzger, G. E. 1967. Some mechanical properties of welds in 6061 aluminum alloy sheet. *Welding Journal* 46(10): 457-s to 469-s.

8. Steenbergen, J. E., and Thornton, H. R. 1970. Quantitative determination of the conditions for hot cracking during welding for aluminum alloys. *Welding Journal* 49(2): 61-s to 68-s.

9. Gittos, N. F., and Scott, M. H. 1981. Heat-affected zone cracking of Al-Mg-Si alloys. *Welding Journal* 60(6): 95-s to 103-s.

10. Katoh, M., and Kerr, H. W. 1987. Investigation of heat-affected zone cracking of GTA welds of Al-Mg-Si alloys using the Varestraint test. *Welding Journal* 66(12): 360-s to 368-s.

11. Kerr, H. W., and Katoh, M. 1987. Investigation of heat-affected zone cracking of GMA welds of Al-Mg-Si alloys using the Varestraint test. *Welding Journal* 66(9): 251-s to 259-s.

12. Miyazaki, M., Nishio, K., Katoh, M., Mukae, S., and Kerr, H. W. 1990. Quantitative investigation of heat-affected zone cracking in aluminum alloy 6061. *Welding Journal* 69(9): 362-s to 371-s.

13. Huang, C., and Kou, S. 2000. Partially melted zone in aluminum welds — liquation mechanism and directional solidification. *Welding Journal* 79(5): 113-s to 120-s.

14. Huang, C., and Kou, S. 2001. Partially melted zone in aluminum welds — solute segregation and mechanical behavior. *Welding Journal* 80(1): 9-s to 17-s.

15. Huang, C., and Kou, S. 2001. Partially melted zone in aluminum welds — planar and cellular solidification. *Welding Journal* 80(2): 46-s to 53-s.

16. Pepe, J. J., and Savage, W. F. 1967. Effects of constitutional liquation in 18-Ni maraging steel weldment. *Welding Journal* 46(9): 411-s to 422-s.

17. Pepe, J. J., and Savage, W. F. 1970. Weld heat-affected zone of the 18Ni maraging steels. *Welding Journal* 49(12): 545-s to 553-s.

18. *Aluminum Standards and Data, p.15*. 1982. Washington D.C.: The Aluminum Association.

19. Huang, C., Kou, S., and Purins, J. R. 2000. Liquation, solidification, segregation and hot cracking in the partially melted zone of Al-4.5Cu welds. *Proceedings of Merton C. Flemings Symposium on Solidification Processing*. p. 229. Edited by R. Abbaschian, H. Brody, and A. Mortensen. Warrendale, Pa.: The Mineral, Metals and Materials Society.

20. Hatch, J. E. 1984. *Aluminum - Properties and Physical Metallurgy*, pp. 64–79. Materials Park, Ohio: ASM International.

21. Philips, H. W. L. 1959. *Annotated Equilibrium Diagrams of Some Aluminum Alloy Systems*, pp. 21–86. London, England: The Institute of Metals.

22. *Metals Handbook*, 1972. Vol. 7, 8th ed., pp. 241–272. Materials Park, Ohio: ASM International.

23. Mondolfo, L. F. 1976. *Aluminum Alloys Structure and Properties*, pp. 717–857. Boston, Mass.: Butterworth.